



**CHALMERS**  
UNIVERSITY OF TECHNOLOGY

## **Al–Mn–Cr–Zr-based alloys tailored for powder bed fusion-laser beam process: Alloy design, printability, resulting microstructure and alloy**

Downloaded from: <https://research.chalmers.se>, 2024-03-13 08:51 UTC

Citation for the original published paper (version of record):

Mehta, B., Nyborg, L., Frisk, K. et al (2022). Al–Mn–Cr–Zr-based alloys tailored for powder bed fusion-laser beam process: Alloy design, printability, resulting microstructure and alloy properties. *Journal of Materials Research*, 37(6): 1256-1268. <http://dx.doi.org/10.1557/s43578-022-00533-1>

N.B. When citing this work, cite the original published paper.



# Al–Mn–Cr–Zr-based alloys tailored for powder bed fusion-laser beam process: Alloy design, printability, resulting microstructure and alloy properties

Bharat Mehta<sup>1,a)</sup> , Lars Nyborg<sup>1</sup>, Karin Frisk<sup>1,2</sup>, Eduard Hryha<sup>1</sup>

<sup>1</sup> Department of Industrial & Materials Science, Chalmers University of Technology, Rännvägen 2A, 412 96 Göteborg, Sweden

<sup>2</sup> Höganäs AB, Höganäs, Sweden

<sup>a)</sup> Address all correspondence to this author. e-mail: bharat.mehta@chalmers.se

Received: 11 November 2021; accepted: 28 February 2022

This study introduces a family of unique Al–Mn–Cr–Zr-based aluminium alloys illustrated by two ternary and one quaternary variants. The choice of alloy compositions has created a system resistant to solidification cracking while retaining high amount of solutes in solid solution in as-printed condition. Good relative density (~99.5%) has been demonstrated along with microstructural study supported by X-ray diffraction to display solidification structure with nanometric precipitate formation in small amounts in as-printed condition. High levels of Mn and Cr produce significant solid solution strengthening reaching hardness of up to 102 HV in as-printed condition. Additionally, the combination of Mn, Cr and Zr is shown to be important to control precipitation strengthening upon direct ageing and coarsening resistance due to slow diffusivity. To elucidate the concept of precipitation strengthening, one set of alloys was aged at 678 K between 0 and 10 h and microhardness results showed that average hardness response reached 130 HV for the quaternary alloy.

## Introduction

Aluminium (Al) is the most abundant metal on the earth's crust and is the second most mined metal after iron [1]. It is completely recyclable and as of 2010, about 30% of the total aluminium produced comes from recycled aluminium [2]. This combined with its low density and high specific strength (via alloying with suitable elements) makes aluminium quite lucrative for structural applications requiring low weight. Aluminium is also known for various secondary properties, such as high thermal and electrical conductivity making it suitable for applications requiring heat loss or electrical conductivity along with high specific strength. Due to such tuneable properties achieved through alloying, aluminium can be found in anything starting from a small soda can to a large aircraft.

Additive manufacturing (AM) is a disruptive and unconventional technology wherein by selective melting of a material, three-dimensional objects can be created directly from design files with limited wastage. Powder bed fusion-laser based (PBF-LB) has gained attention recently for its potential to manufacture defect-free parts in a variety of materials and can have

properties better than the conventionally cast counterparts [3, 4]. The PBF-LB process can create components by rapidly melting and solidifying the material which is in the form of a thin powder layer (usually 20–60 µm) to solid components. This is then repeated by the re-melting and reheating of previously solidified layers, thus, forming a complex microstructure. This complicated process, thus, creates the need for new or modified material compositions. Not only can the processability of alloys be improved, but whole new paths of alloy design can be opened, which have not been possible before. For aluminium alloys, in particular, this has been shown by several authors [5, 6] where they have shown that extension of solid solubility away from the equilibrium is possible by alloying aluminium with elements such as Mn, Zr and Sc. If standard alloys are used, such as Aluminium 6061/7075, this can lead to two issues in PBF-LB: severe solidification cracking and evaporation of low melting elements such as Zn or Mg [7, 8]. Some researchers have addressed the solidification cracking issue by modifying the solidification process of aluminium by creating alternate solidification paths for Al-grains by providing nucleants (such as Al<sub>3</sub>(Sc,Zr) or TiB<sub>2</sub>)

[7, 9], whereby the formation of columnar Al-grains is avoided by breaking them up into smaller equiaxed grains. Another way could be to develop grades of aluminium alloys that are less prone to solidification cracking owing to inherent lower solidification cracking susceptibility [10, 11]. The latter approach can be realised by understanding the segregation behaviour of solutes based on thermodynamic calculations with tools such as Scheil solidification predictions, thereby, developing compositions that are less segregation sensitive to create cracking resistant alloys [12]. Clearly, the combination of extended solid solubility and control of segregation behaviour upon solidification could be key to developing new alloys for PBF-LB.

The solution, thus, lies in completely new compositions of Al alloys, which use different elements than the conventionally used ones such as Si, Mg, Cu or Zn. These new compositions are possible by utilising the transition series elements such as Fe, Cr, Ni and Co of which solubility can be extended by up to two orders of magnitude via rapid solidification [13]. Additionally, further strengthening post-processing is shown by precipitation strengthening enabled via direct ageing heat treatments. The goal of this alloy design work is to create alloys with > 400 MPa ultimate tensile strength (UTS) which are stable at high temperatures (up to 473–523 K).

## Results

The results section is divided into four sub-sections namely *alloy design, printability of alloys, resulting microstructure and alloy properties*.

### Alloy design

It is estimated that the PBF-LB processing involves cooling rates in range of  $10^3$  to  $10^5$  K/s [14]. This provides alloy designers the opportunity to assume higher supersaturation of elements in Al-matrix during the processing of the alloys [15]. The alloying elements used in this study were selected based on research conducted on rapidly solidified material where the benefit of transition metal elements into the solid solution of aluminium alloys was discussed [13, 15–17]. It has been shown that transition elements such as Mn, Cr, Fe and Ni could be game changers if their solubility could be increased in Al alloys, since they add high misfit strains to Al-matrix. Of particular interest are Mn, Cr which have with low bulk diffusivities, thus, having a high potential of solid solution strengthening and high-temperature strengths when forming secondary precipitates via direct ageing. As a result, using atomisation process [18] combined with hot extrusion manufacturing, Al–5Mn–2.5 Cr (wt%) powder grades were created by researchers in Sweden during 1980s. It was shown that such alloys were temperature resistant and retained hardness up to 523 K [19, 20]. Other researchers have

also suggested a limit of solubility based on rapid solidification process and cooling rates which are applicable for gas atomisation process and PBF-LB process [13, 20–22]. For example at cooling rates of  $10^3$  to  $10^4$  K/s, the solubility of Cr and Mn in Al reaches 3–6 wt% and 6–8 wt%, respectively. In comparison with the maximum equilibrium solubility at the melting temperatures, 0.8 wt% for Cr and 1.8 wt% for Mn [23], this is a large increase in solubility. As a further tool in selecting alloy compositions, CALPHAD simulations were performed by suppressing the formation of primary precipitates, which are usually formed during via slow cooling methods such as casting, as shown in Fig. 1(a)–(c). In Fig. 1(c), suppressing the primary Al<sub>3</sub>Zr precipitate (Al<sub>3</sub>Zr\_D023) shifts the solvus lines to the right (dotted lines show equilibrium state and solid lines show non-equilibrium state). This means a higher solubility can be achieved in Al-matrix (0.5 wt% Zr instead of 0.25 wt% Zr at equilibrium). Similar trend is seen for Al–Mn and Al–Cr in Fig. 1(a) and (b), respectively. Furthermore, this solubility can be increased by an extended cooling rates as the time available for formation of the primary precipitate or even the metastable precipitate can be reduced, leading to a solid solution with higher solubility as shown visually in Fig. 1(d). This means that depending on the cooling rate, the solubility seen at a higher temperature (such as 2 wt% Zr solubility if cooling rates >  $10^4$  K/s) can be realised after solidification.

Moreover, Al–Mn–Zr [25] and Al–Cr–Zr [22] alloys manufactured via melt spinning have shown high hardening post-processing, reaching hardness as high as 200 HV. Thus, based on the cooling rate limits which are applicable for both PBF-LB processing and atomisation processing combined with lucrative hardening response, Mn, Cr and Zr were selected for alloying. This resulted in formation of the first batch of atomised alloys, with three compositions, namely alloy A, B and C as shown in Table 1. Alloy A and B are designed as ternary alloys Al–Mn–Zr based and Al–Mn–Cr based, respectively, whereas alloy C is a quaternary Al–Mn–Cr–Zr-based alloy. This was done in order to separate out the effects of each alloying element, both in terms of their solubility in matrix and precipitation hardening capability. The alloys that have been developed contain about three times higher amount of solutes than the solubility limits of Mn, Cr and Zr combined at equilibrium solubilities at melting temperatures [23]. This is considered as a big advantage of PBF-LB processing wherein rapid solidification process can lead to higher solubility. For the selection of amount of alloying elements, Cr was kept close to equilibrium amount (0.77 wt%), Zr was boosted to an amount known to be possible in PBF-LB [6] and Mn was increased based on literature evidence for rapidly solidified materials [15, 20, 25]. It was estimated that this will provide a big elevation in solid solution strengthening from these elements, especially Mn and Cr. The estimated potential increase

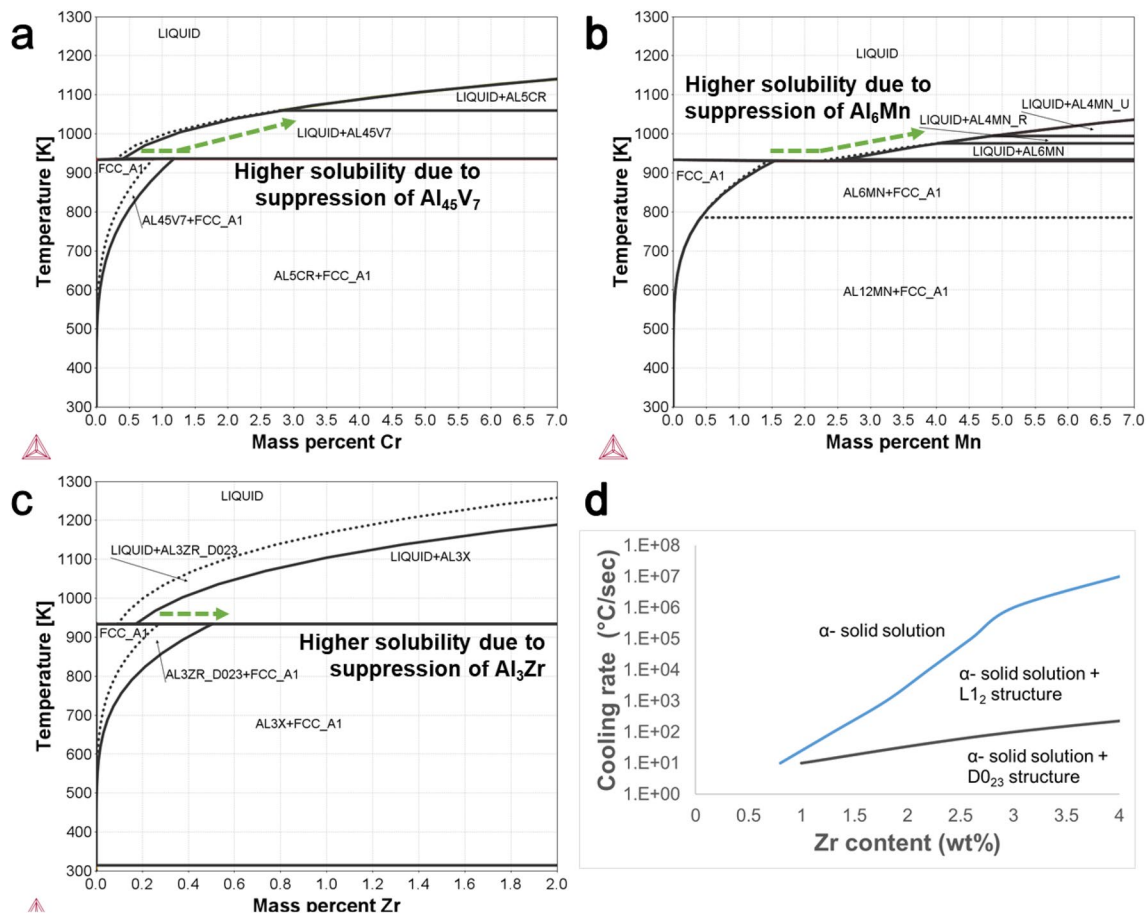


**Figure 1:** (a) Al–Cr equilibrium and non-equilibrium binary phase diagram showing the change in solubility upon suppression of primary Al<sub>45</sub>V<sub>7</sub> precipitate (b–c) Similar phase diagrams for Al–Mn and Al–Zr, respectively, showing change in solubility upon suppression of primary precipitates, namely Al<sub>6</sub>Mn and Al<sub>3</sub>Zr\_D023. Dotted lines represent equilibrium solvus lines and solid lines represent non-equilibrium lines after suppression of respective primary precipitates. Drawn using ThermoCalc2021a with TCAL7 database. (d) Interrelation among cooling rate, zirconium content and solidified structure in Al–Zr alloys, recalculated and redrawn from [24].

**TABLE 1:** Alloy compositions for novel Al–Mn–Cr–Zr alloys.

Alloy name	Condition	Alloy composition (in wt%)
Alloy A	As-atomised	Al 4.7 Mn 0.48 Zr 0.15 Fe 0.16 Si
	As-printed	Al 4.8 Mn 0.47 Zr 0.16 Fe 0.16 Si
Alloy B	As-atomised	Al 5.0 Mn 0.8 Cr 0.14 Fe 0.16 Si
	As-printed	Al 4.9 Mn 0.8 Cr 0.18 Fe 0.17 Si
Alloy C	As-atomised	Al 5.0 Mn 0.8 Cr 0.59 Zr 0.16 Fe 0.16 Si
	As-printed	Al 5.0 Mn 0.8 Cr 0.60 Zr 0.16 Fe 0.17 Si

The alloys were tested for chemical analysis using ICP-AES technique.

in yield strength owing to addition of Mn, Cr and Mg in solid solution was also calculated. The estimated strengthening was based on first-principle calculations done on binary Al alloys, showing expected increase in yield strength for solid solution coming from the misfit strain generated by solutes ( $\epsilon$ ) and concentration of solutes in the matrix ( $c$ ) [17, 26]. This means

that a total of 5.8 wt% (Mn + Cr) could potentially provide an increase in solid solution strengthening of ~ 300 MPa whereas a similar amount of Mg in solid solution will result in ~100 MPa. A plot representing the tentative solid solution strengthening effect of Mn, Cr and Mg is provided in Fig. S6 in online resource. Furthermore, Al<sub>5</sub>Mn<sub>2.5</sub>Cr alloy system was shown in literature to have a precipitation strengthening response on direct ageing between 573 and 673 K [19, 20], tentatively from Al<sub>12</sub>(Mn,Cr) semi-coherent precipitates. The Zr used in the alloys is based on extensive literature review wherein Zr in solid solution can lead to strong precipitation hardening after direct ageing around similar temperatures of 623–723 K [6, 27] via formation of nanometric Al<sub>3</sub>Zr precipitates. The extended Zr solubility can result in up to 30–35 HV increase from these Al–Zr precipitates upon ageing [6]. The effect of each alloying element is discussed in further detail in following sections. The alloys were also seen to contain some Fe, Si (<0.2 wt%) as unavoidable impurities from the atomisation process.

The second important criterion for alloy design which was considered together with the extension to solubility was to limit the tendency for solidification cracking. The resistance to solidification cracking was tested using Scheil solidification curves. It was done for four alloys, two commercial conventional alloy grades namely Al-7075 and Al-6061, commercial PBF-LB alloy namely AlSi10Mg and one of the novel Al alloy namely Alloy C. The Scheil curves developed were then redrawn as presented in and used for calculating the maximum  $\left| \frac{dT}{d(f_s^{1/2})} \right|$  slope close to the end of solidification (when  $(f_s)^{1/2} \sim 1$ ) and the solidification range where mass fraction of solid ( $f_s$ ) is between 0.8 and 1. Composition of different alloys and calculated value for slopes are provided in Tables S2 and S3 in online resource. The alloy C as a prototype for the novel alloy design has negligible slope close to the solidification similar to AlSi10Mg, while the Al-6061 and Al-7075 have substantially higher slopes, about one order of magnitude higher. The values are expected to reflect the solidification cracking susceptibility (Fig. 2).

Moreover, the small slope formed at the end of solidification in alloy C is due to the presence of Fe, Si as impurities in the alloy. This fact was included in alloy design itself as it was expected that addition of such low amounts did not affect printability and not form significant amount of precipitates. Figure S3 in online resource shows how 0.15 wt% each Fe, Si has negligible effect to Scheil solidification curve in alloy C. It is only when this amount reaches 1 wt% each that the effect to the solidification behaviour becomes a factor to consider while designing such Al alloys.

### Printability of alloys

The results from design of experiments (DOE) approach to achieve high relative density are represented in Fig. 3(a)–(d). This was tested by conducting a modified version of two-level full factorial DOE with centre point runs to achieve a processability

window with high density. Each sample, shown by a black dot, represents the processing parameter used. The relative density was calculated via image analysis of polished samples under optical microscope. More details are provided in the methods section. There were two reasons for conducting a DOE study. First, EOS M100 PBF-LB machine that was used for printing was not optimised for Al alloys; hence, no standard parameters were available. Additionally, to depict the crack resistance of these alloys regions with low relative density (92–94% relative density) achieved via low or high energy density had to be printed without cracks. While conducting DOE for alloys A and B, two variables were considered namely hatch distance and laser speed to obtain high density regions, as seen in Fig. 3(a) and (b). The laser power and layer thickness were constant at 170 W and 0.03 mm, respectively. When testing alloy C, a more extensive DOE was conducted with laser power as a third variable while layer thickness was constant at 0.03 mm. Figure 3(c) and (d) shows that a more descriptive processing window was, thus, obtained and this was considered as a good starting point for achieving good density. For all the three alloys, the processing parameters with 170 W power, 1500 mm/s laser speed, 0.1 mm hatch distance, and 0.03 mm layer thickness were seen to provide good relative density (99.5–99.6% in best case of Alloy C), and these were selected as the optimum processing parameter settings.

Optical microscopy was used to do relative density measurements, as summarised in Fig. 3(a)–(d). Additionally, the same images were used to detect solidification cracking and no cracks were observed in any of the samples printed. As an illustration, Fig. 4 shows the cross section for alloy C at optimised processing parameters for all three cut sections in as-printed state. No cracking was seen in the sample, and quite clean samples were seen. When analysing all samples from the DOE studies, two types of common defects were recognised as observed in other studies for PBF-LB of aluminium alloys [11, 29, 30]. Some low magnification images for the different defects seen during DOE studies are illustrated in Fig. S4 in online resource.

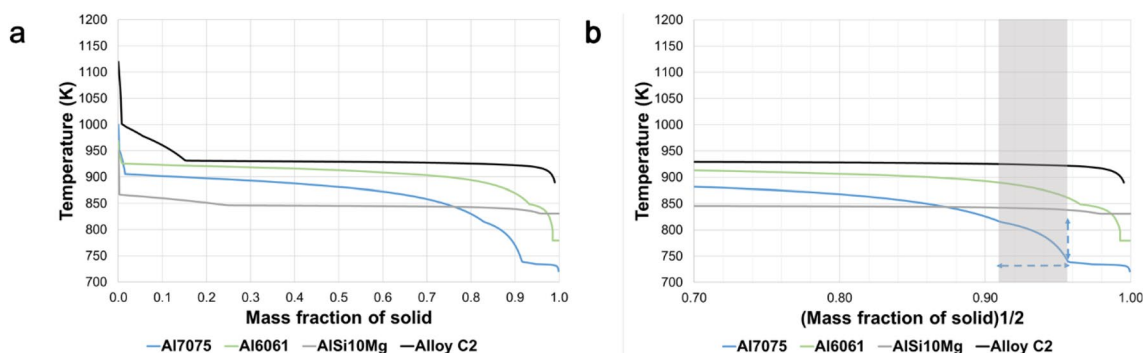


**Figure 2:** (a) Scheil solidification curve for different Al alloys across the whole solidification range. (b) Scheil solidification curve when  $(\text{mass fraction of solid})^{1/2}$  is close to 1. The steepness of curve is illustrated for Al-7075. Calculations done using ThermoCalc v2021a software using TCAL7 and MOBALS database.



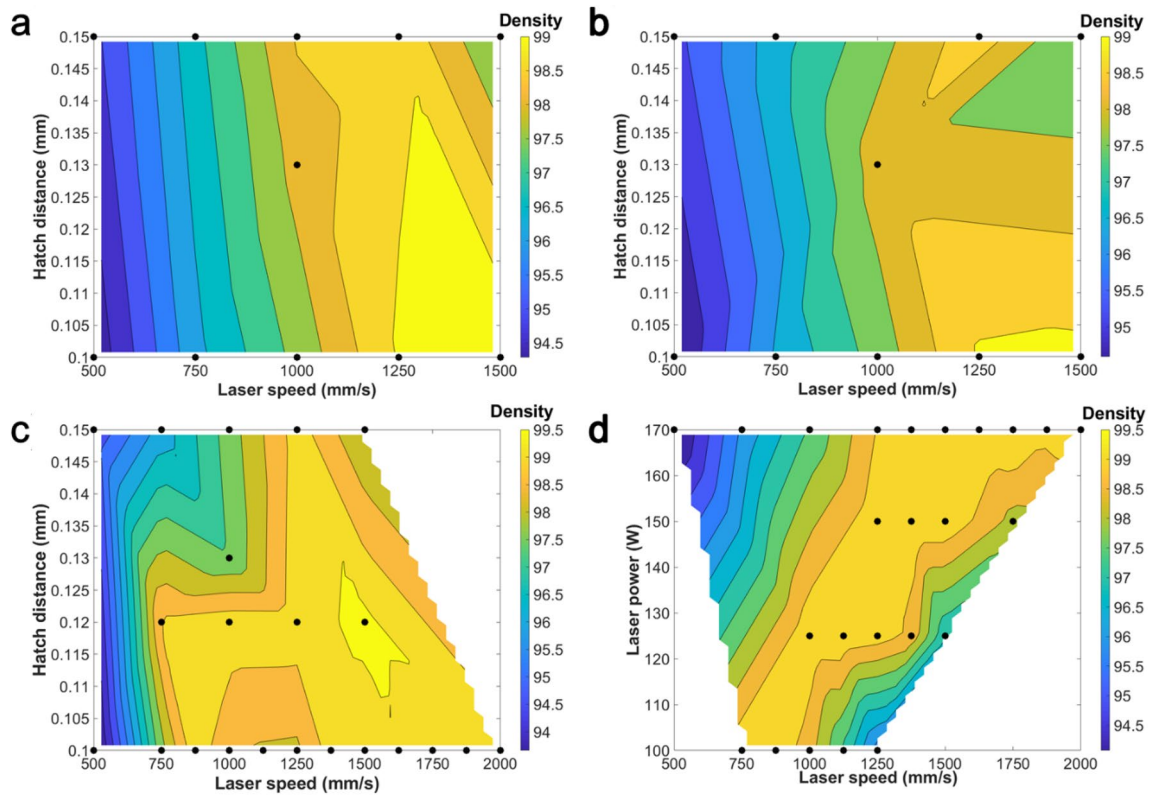


**Figure 3:** Contour plots showing relative density (%) achieved by (a, b) Varying laser speed (mm/s) and hatch distance (mm) in alloy A,B respectively; (c) Varying laser speed (mm/s) and hatch distance (mm) for alloy C and (d) Varying laser speed (mm/s) and laser power (W) for alloy C. Plots drawn using curve fitting tool in MATLAB 2021a software with interpolant method and linear curve fitting setting.

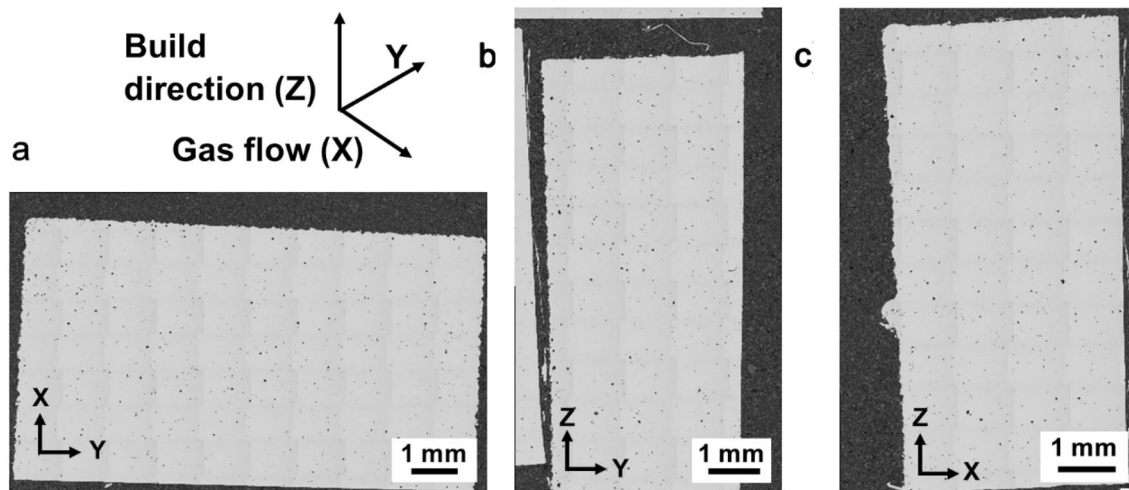


**Figure 4:** Schematic shows the three different directions (X, Y, Z) for printing. Low-magnification optical microscopy images showing (a) XY plane (b) YZ plane and (c) XZ plane views for Alloy C in as-printed state having about 99.6% average relative density.

### Resulting microstructure

The focus of microstructure studies was kept on the as-printed samples as those were considered to be the ones of interest for actual applications and not the as-atomised powder. However,

to identify the starting point, a few cross sections of as-atomised powder were also studied which showed relatively dendritic solidification structure with negligible precipitation. Few precipitates in the inter-dendritic regions of sizes < 100 nm were

seen. The electron microscopy images for the same are shown in Fig. S5 in online resource. The as-printed samples were characterised in the SEM in backscattered mode (BSE) in as-polished condition, to be able to recognise grain contrast easily. Additionally, BSE helped with detecting the precipitates (if any) by higher contrast compared to the Al-matrix. The images along XZ plane and XY plane are shown in Fig. 5 for alloy C. The figure shows columnar grain structure along the build direction with finer grains along XY plane. All the alloys showed similar

grain morphology with negligible precipitation visible at low magnifications.

On further investigation of the XZ plane at high magnifications, it was observed that two different categories of nanometric precipitates formed in the alloy in the as-printed condition were characterised by their morphology and location in the sample:

1. Precipitates located at melt pool boundaries
2. Precipitates located at grain/cell boundaries

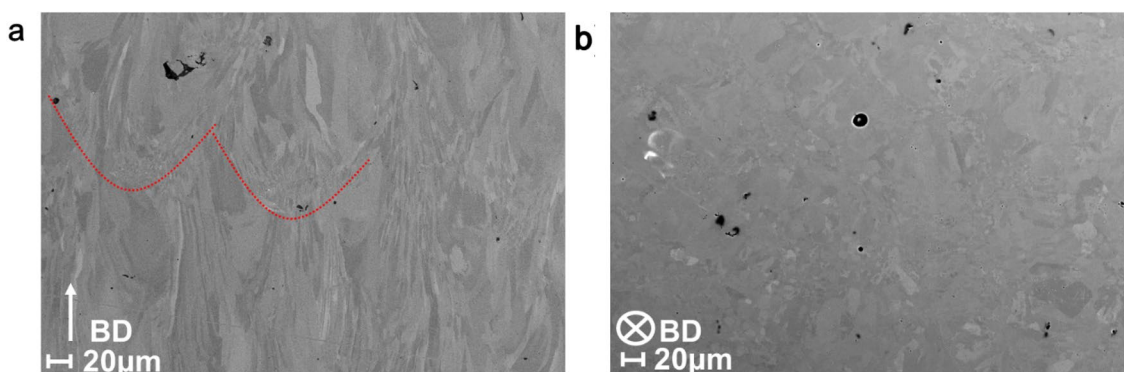


**Figure 5:** Electron microscopy image of Alloy C (as-printed) along (a) XZ plane with building direction from bottom to top and melt pool boundaries marked in red (b) XY plane with build direction inwards from image.

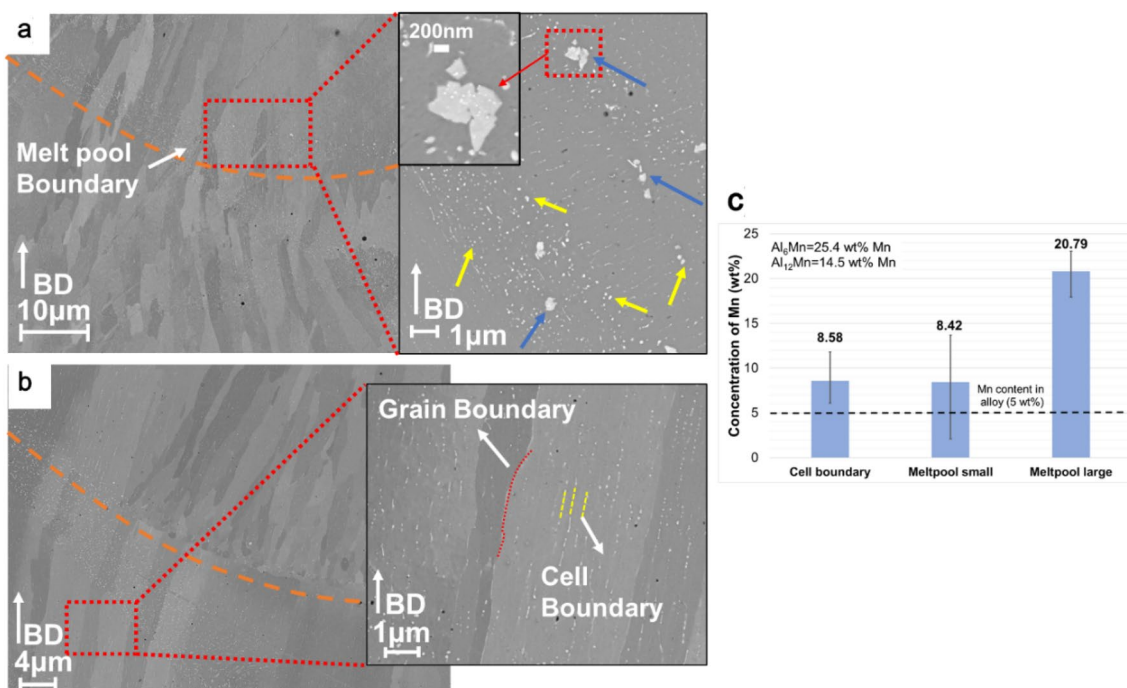


**Figure 6:** Electron microscopy image of Alloy C in as-printed state showing two different melt pool boundary regions (orange) in (a), (b). (a) Magnified region with precipitates detected at melt pool boundary region on basis of size (as small marked yellow and large marked blue). Large precipitates are shown in high magnification in the inset in (a). (b) Magnified region with precipitates detected at grain boundary and cell boundary regions (c) EDS Chemical analysis of three categories of Mn-containing precipitates depicted for alloy C in as-printed state; cell boundary precipitates, small and large precipitates at melt pool boundaries. All these precipitates are enriched in Mn.

The precipitates located at melt pool boundaries are shown in Fig. 6(a) where it can be seen that these precipitates have two typical sizes: smaller ones with spherical morphology and average sizes <100 nm and larger ones between 200 and 400 nm in size. The second category of precipitates was those forming at grain and cell boundaries, as seen in Fig. 6(b). Their shape was rod like with length of 200–400 nm and small diameter (< 50 nm). These particles aligning themselves along grain/cell boundaries suggest that the precipitates are formed during solidification. Figure 6(c) shows the summary based on EDS point scans of these two types of precipitates. The EDS has much larger uncertainty for smaller particles due to the interaction volume generated by electron beam of the SEM as compared to the volume of precipitate, even if low accelerating voltage of 4 kV was applied here to limit the interaction volume. However, to compensate for this, a high number of point scans (> 25) at high resolution were done to get a relatively consistent results. The results suggested that the smaller melt pool boundary and grain/cell boundary precipitates were richer in Mn than the matrix concentration of Mn (5 wt%), but it could not be indicated if they could be either of  $\text{Al}_{12}\text{Mn}$  or  $\text{Al}_6\text{Mn}$  stoichiometry. The larger melt pool boundary precipitates, however, were suggested to have a  $\text{Al}_6\text{Mn}$  stoichiometry, thus, supporting the results shown later from XRD analysis.

## Alloy properties

### X-ray diffraction

The X-ray diffraction was conducted on all alloys (A, B, C) in their as-atomised and as-printed condition to detect minor precipitates (if any) and calculate the amount of supersaturation via observing the shift in Al peak with respect to pure Al. It was done on the as-printed samples with optimal processing

parameters established before. In the XRD plots presented in Fig. 7, it was observed that all the alloys show similar information from the peaks, except a peak shift for Al when comparing alloy A to alloy B/C. The Al peaks were seen to be shifted to a higher angle ( $2\theta$ ) as compared to the positions expected for pure Al, which are attributed to solutes dissolved in solid solution. Minor peaks observed in all alloys around  $40.4^\circ$  and  $43.0^\circ$  (see inset view in Fig. 7(a) are attributed to few nanometric Al-Mn precipitates (shown in the literature as  $\text{Al}_6\text{Mn}$  or  $\text{Al}_{12}\text{Mn}$  [20, 21, 28]), which have also been confirmed via SEM analysis. Figure 7(b) presents an attempt to correlate the solubility in the alloy as a sum of effects of alloying elements on lattice parameters with the Al peak shift. This was done by utilising a ‘rule of mixtures’ approach, where the effect of each element was taken from the literature, based on first-principle calculations for binary Al alloys [17]. The only modification made to those calculations was that the starting point of pure Al was modified to  $4.0478 \text{ \AA}$  (PDF nr. 0040787), instead of  $4.016 \text{ \AA}$  as assumed in Ref. [17], because this value was seen to be much more reliable as per DIFFRAC.SUITE EVA software. More information on this method is provided in Fig. S7 in online resource. The values were then verified against the experimental values derived from the strongest Al peak which was at around  $45^\circ$  in as-printed samples and around  $39^\circ$  in as-atomised samples, as shown in Fig. 7(b). It can be observed that the experimental and theoretical lattice parameters are within  $0.01 \text{ \AA}$  and show a similar trend.

### Direct ageing and hardness response

After proving the solid solution capabilities, microhardness testing was conducted on the samples with optimal processing parameters established before to indicate strengthening from dissolved solutes. It was seen that Alloys A, B and C show average hardness values of 91, 99 and  $102 \text{ HV}$ , respectively, which

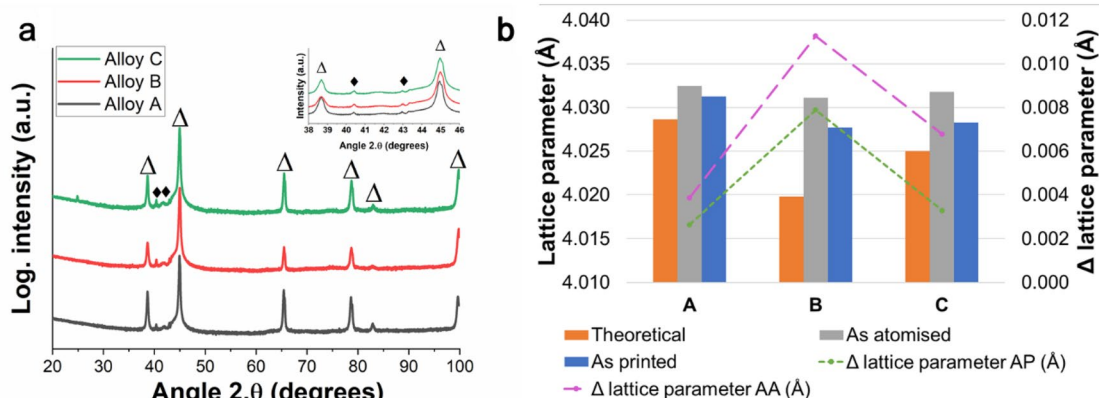


**Figure 7:** (a) X-ray plots for all alloys in as-printed condition. Inset shows the formation of minor peaks, attributed to Al-Mn precipitates  $\Delta$ =pure-Al peaks and filled diamond = Al-Mn precipitate peaks. (b) Lattice parameter values based on X-ray diffraction patterns for all four alloys in as-atomised and as-printed conditions. The  $\Delta$  lattice parameters reflect the difference between theoretically calculated values to as-atomised (AA) and as-printed (AP), respectively. X-ray diffraction conducted at 298 K.



is much higher than pure Al of 20 HV. One set of as-printed samples from all alloys was aged to 678 K to demonstrate age hardenability and one set of as-printed samples from alloys A, C were heat treated at 523 K to show the inherent resistance to high temperature right after printing. Figure 8(a) and (b) shows the age-hardening response of the Al alloys after heating at 678 K for up to 10h and hardness properties of alloys A and C, after heating at 523 K, respectively.

## Discussion

The approach to alloy design of Al alloys tailored for PBF-LB process taking into account specifics of powder fabrication and PBF-LB processing to eliminate solidification cracking [7, 8, 31] were addressed in the present study. This problem was resolved by basing the alloy composition to include elements that are less prone to segregation during solidification. The solidification cracking can be depicted to arise from shift in concentration gradients in the liquid as solidification occurs, thus, leading to higher solute content in the last liquid, causing higher volumetric shrinkage when this liquid solidifies [7]. These cracks can form between solidifying grains and span several grains. According to Kuo [10], this can be solved by lowering the solidification range, in particular in the range of the last solidifying melt ( $f_s \sim 1$ ). This means that there is minimum temperature gradient, thus, ensuring good amount of liquid metal available for bonding along two grain boundaries and avoiding crack formation. Following Scheil solidification curves, it was shown (in Fig. 8) that the solidification cracking susceptibility for the novel Al alloys in this respect is significantly reduced. All the printed samples supported this cracking resistance, and thus, an “inherently crack-free” material is obtained. The concept of higher supersaturation enabled due to PBF-LB processing has been illustrated via the XRD plots for all alloys in Fig. 6, which suggests very little precipitation in the as-printed condition due to a very small minor phase corresponding to Al-Mn formed. This has also been verified with SEM analysis, where only

limited nanometric precipitation (as shown in Fig. 5) was seen in as-printed condition. Additionally, the peak shift for Al peaks suggests a high supersaturation of dissolved elements and the lattice parameters obtained experimentally are close to the suggested parameters obtained in the literature for rapidly solidified Al-Mn and Al-Mn-Cr alloys [20, 21]. These parameters were also tested against theoretical lattice parameter values where values for Mn, Cr and Zr addition were taken based on study by Uesugi et al. [17] wherein lattice misfit and concentration in matrix are used to measure theoretical lattice parameter. The differences in theoretical and experimentally obtained parameters were seen to be within 0.01 Å, which could be explained by small amount of precipitation. Thus, such a method of testing theoretically calculated lattice parameter values that need more work, as it may not be able to include effects of precipitation, texture in material, etc. Furthermore, as-printed microhardness of all alloys suggests reasonable strength in as-printed condition [as compared to pure Al (20 HV)], thus, supporting high supersaturation and solid solution strengthening in the Al-matrix. The strength of these alloys in as-printed state is, thus, attributed as a mix of solid solution strength and possibly some grain refinement strengthening. The effect of grain refinement on mechanical properties in Al alloys is very weak as compared to Ni or Fe [33]. For example: In case of pure Al, a refinement of average grain sizes from 100 µm to 1 µm would result in about 61.5 MPa increase in yield strength, whereas the same effect increases to 157 MPa and 212 MPa in Ni and Fe, respectively. A detailed visual representation is shown in Fig. S8 in online resource. Thus, grain refinement was considered as a secondary strengthening effect for these alloys.

The microstructure of this material as seen in Fig. 4 is typical microstructure seen in PBF-LB-processed materials with columnar grains along build direction [11, 30]. The grain refining  $L1_2$  form of  $Al_3Zr$  precipitates was not observed during microstructural analysis, which is usually observed in Zr-containing Al alloys. Croteau et al. [6] have suggested that the precursor for such precipitates to form is the presence of Mg in

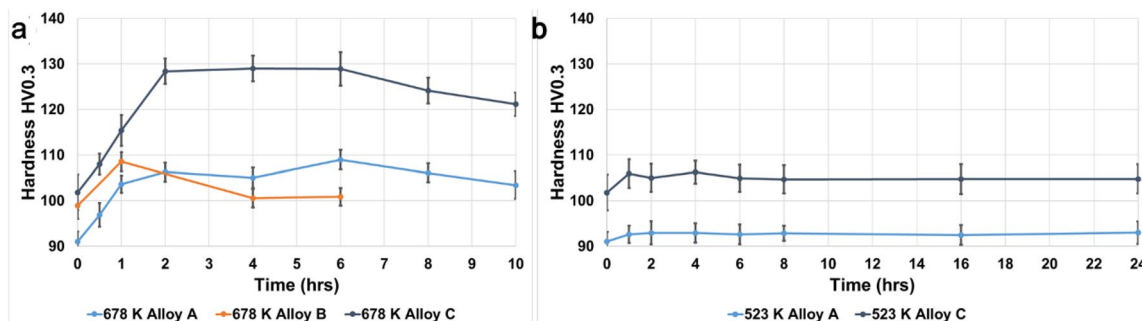


**Figure 8:** Microhardness map for (a) all three Al alloys after being aged at 678 K for 0.5–10 h and (b) alloys A and C after heated at 523 K for between 1 and 24 h.

the alloy, which oxidises as MgO, which then results in the formation of the  $\text{Al}_3\text{Zr}$  cubical phases. Hence, future alloy iterations may be developed with some Mg content in order to develop grain refinement if necessary. Upon observing the microstructure under high magnification as shown in Fig. 5, nanometric precipitates were observed rich in Mn. They were observed as melt pool boundary precipitates or solidification (grain/cell) boundary precipitates. XRD results suggest minor peaks corresponding to  $\text{Al}_{12}\text{Mn}$  or  $\text{Al}_6\text{Mn}$  (as seen in Fig. 6). However, it is hard to quantify the exact amount of these minor precipitates as the peak intensity ratio is low ( $< 5 \text{ vol}\%$ ). Since re-melting of layers and segregation of primary precipitates along the solidification front during processing is fundamental to the process itself, formation of precipitates may be possible to reduce in size, but it may be impossible to be avoided completely in the as-printed state for this level of Mn content. The segregation of Mn along grain boundaries has been shown experimentally in rapidly solidified and nanocrystalline Al–Mn-based alloys by other authors [21, 34, 35], suggesting also that higher concentrations of Mn may lead to formation of ‘quasicrystalline’ phases, which are metastable phases. The precipitates at melt pool boundaries are analogous to inclusions forming during welding of metals at the heat-affected region. In Fig. 5, it is shown that the precipitation is expected to occur at the zone right below the remelted region in the previously deposited layer. There would be a clear driving force for this to occur as the equilibrium solubility for Mn is about 1.8 wt% and these alloys have about 5 wt% Mn available in the supersaturated solid (in previously deposited layer). The large melt pool boundary precipitates are seen to have an  $\text{Al}_6\text{Mn}$  stoichiometry, although their crystal structure is not known in the initial investigation. Both the smaller melt pool boundary precipitates and grain/sub-grain boundary precipitates have higher Mn content than the matrix (8.42 wt% and 8.58 wt% respectively), seen in Fig. 5(c), which is indicative of Mn enrichment. Their exact stoichiometry and crystal structure need to be confirmed via transmission electron microscopy (TEM) later.

The effect of direct ageing on all the alloys is shown in Fig. 7(a) and (b) via microhardness maps across various times and temperatures. Upon direct ageing, precipitation strengthening is expected as the major source of strengthening, where solutes diffusing out of Al-matrix assist the growth of precipitates such as Al–Mn containing or Al–Zr containing. It is believed that nanometric Al–Zr precipitates provide the highest strengthening in these alloys, similar to a 30 HV increase observed in Al–Mg–Zr-based alloys [6]. Al–Mn-containing precipitates are also shown to have a definite strengthening effect, but their precipitation kinetics need to be studied in further detail to optimise the hardening behaviour. At relatively lower temperatures as seen in Fig. 7(b), negligible hardness increases in alloy A, C up to 24 h at 523 K, which is supported by the

alloy design approach of selecting elements with low bulk diffusivities, thus, having slow precipitation kinetics. It has been shown in the literature that Mn, Cr and Zr have bulk diffusivities lower than conventional alloying elements such as Mg and Cu by several orders of magnitude [27, 32] which could play a key role in resistance to precipitation. When ageing was conducted at relatively higher temperatures of 678 K as shown in Fig. 7(a), it was seen that alloy A and C produced a consistent hardening effect lasting between 2 and 6 h followed by reduction in peak hardness. The starting point for alloy A and alloy C is different due to 0.8 wt% Cr in solid solution, improving the starting point from 91 to 102 HV from alloy A to alloy C, respectively, which is a big contribution. The precipitation strengthening in both these alloys is attributed mainly to Zr present in solid solution, known to form nanometric  $\text{Al}_3\text{Zr}$  precipitates which are metastable and coherent to Al-matrix and provide high strengthening potential [6, 27, 36]. Although Zr is seen as a primary strengthening precipitate, when comparing the strengthening to Zr-free alloy which is alloy B in Fig. 7(b), it is seen that some hardness increase is produced for 1 h which is quickly followed by reduction in hardness, suggesting overageing occurring rapidly. This, however, indicates that Al–Mn-containing precipitates, as suggested to form in Fig. 5 could be growing in a favourable way to cause strengthening. Second, it is only after adding Cr in the alloys as a comparison between alloy A and C, the ageing response becomes more pronounced and a larger increase in hardness is achieved (18 HV and 28 HV as maximum increase in hardness in alloy A and alloy C, respectively). Based on literature evidence, it is believed that this is due to formation of hardening  $\text{Al}_{12}(\text{Mn}, \text{Cr})$  precipitates, wherein Mn is replaced by Cr, which is slower in diffusivity, thus, slowing the precipitation kinetics of this precipitate [19, 20, 34].

## Conclusions

This study introduces a method of alloy design (elucidated with a family of Al–Mn–Cr–Zr-based alloys) tailored for PBF-LB to create crack-free and tentatively high-performance alloys based on the combination of solid solution and precipitation strengthening. It is supported by thermodynamic modelling where the processability of the alloys can be tuned to have high amount of solutes in solid solution, while avoiding the common solidification cracking phenomenon. In this study, the authors present that Mn, Cr and Zr combined could provide one such alloy system wherein solidification cracking phenomenon is completely avoided, creating “inherently crack-free” materials. Low susceptibility to solidification cracking is demonstrated as supported by printing crack-free 10 mm side cubes. Full dissolution of 0.8 wt% Cr and 0.5–0.7 wt% Zr with nearly complete dissolution of 5 wt% Mn ( $< 5 \text{ vol}\%$  precipitates) was shown. The results prove the concept that choosing a safe path for solidification

can be realised if basic understanding of AM processing and powder technology principles are considered. The alloys, thereafter, produced via PBF-LB were shown via a DOE approach to be printable to reach high relative density of 99.5% with good processability window. In as-atomised and as-printed conditions, some segregation along solidification structures such as dendritic/cell boundaries as well as grain boundaries are seen. For as-printed samples, in particular, meltpool boundary precipitation was observed, involving in-process nucleation and formation of Mn-rich nanometric precipitates believed being beneficial rather than being detrimental. Despite their formation, most of the alloying elements are still preserved in solid solution, whereby intended age-hardening response is kept. Further growth of precipitates is consequently also seen to be slow, causing the Al-matrix to strengthen during direct ageing and creating at present medium-high strength alloy for the most alloyed variants (alloy C). Higher amounts of Mn and Cr in the solid solution are shown to enhance solid solution strengthening capabilities, while resistance to precipitation is kept up to 523 K. Second, when precipitation is triggered at higher temperatures (one example is elucidated at 678 K), precipitation strengthening is observed at a relatively slow rate. This could mean that the peak hardness of the alloys could be further improved and high-temperature properties can be expected due to a better control of precipitate growth as outlined in the present study.

## Materials and methods

### Materials

Powder variants were produced by means of nitrogen gas atomisation process, and powder produced was classified to nominal particle size range of 20–53  $\mu\text{m}$ . The powder variants were provided by Höganäs AB. Three powder grades were designed with the final chemical compositions as presented in Table 1. More details about the particle size distribution data etc. are provided in Table S1 and Fig. S1 in online resource.

### Alloy design tools

Tentative phase diagrams (from binary to quaternary) were developed using ThermoCalc software (TCAL7, MOBAL5 database in ThermoCalc v2021a) and possible metastable phase

diagrams were used as indicators for higher dissolution of alloying elements as compared to equilibrium. The second important criterion for alloy design was to choose alloying elements based on Scheil solidification calculations and selected for negligible solidification cracking susceptibility, as defined by Kuo [10]. This approach created an easy pathway for avoiding unnecessary issues during printing such as solidification cracking. The approach could be visualised using Scheil solidification curves, which were developed using ThermoCalc v2021a software using the TCAL7 and MOBAL5 databases.

### PBF-LB processing and design of experiments for establishing full density

The different variants of powder were processed in an EOS M100 machine with a 40  $\mu\text{m}$  spot size, 200 W (170W nominal) power Yb-fibre laser. The samples were initially printed keeping 170 W power and 0.03 mm layer thickness as fixed processing input along with normal scan rotation of 67°. The processability of the materials was tested based on a simple two-level full factorial design with centre point runs to identify the regions of interest with high relative density ( $\sim 99.5\%$ ). This design of experiment (DOE) approach was adopted with hatch distance and laser speed as variable-processing input to identify conditions for high density after printing. A final DOE was conducted for the quaternary alloy (Alloy C) to make a full two factorial three-variable design with laser power as the third variable in the DOE. Table 2 summarises the range of processing parameters used for each alloy in the DOE. The powder samples were conditioned by means of a drying procedure at 353 K for 4 h before every print. The samples were printed as cubes of  $10 \times 10 \times 10 \text{ mm}^3$ . The samples were built with building direction as Z axis, gas flow direction as X axis and third direction as Y axis. The samples were designed with a notch to mark the direction of gas flow in the chamber. More details about the sample design are provided in Fig. S2 in online resource. All the samples were cut with a cold saw after printing from the build plate.

The relative densities of the samples were determined from optical microscopy of cross sections. The sections investigated were taken along three planes (XY, XZ, YZ). To identify and retrieve the porosity, results were then obtained for all three planes and averaged for each sample in order

**TABLE 2:** Summary of processing parameters for design of experiments (DOE) for all four Al alloys.

Alloy	Laser power (W)	Hatch distance (mm)	Laser speed (mm/s)	Total number of samples
Alloy A	170	0.1–0.15	500–1500	13
Alloy B	170	0.1–0.15	500–1500	13
Alloy C	100–170	0.1–0.15	500–2000	46

Layer thickness was kept constant at 0.03 mm for all the samples.

to minimise effect of orientation for the overall porosity values reported. The image analysis was done by using ImageJ software and sections of each sample having approximately 100–150 mm<sup>2</sup> total scanned area per sample.

### Microstructure evaluation and mechanical testing

All the samples were prepared by cutting them close to the centre of all three followed by mounting them in an epoxy-based thermoset resin, called Polyfast (from Struers). This was followed by grinding the samples with 200, 500, 800, 1000 and 4000 foils followed by polishing the samples with 1 µm diamond-based polish and final step with OP-S silica suspension on a Struers TegraPol 31 machine. Samples were etched using standard Keller's reagent for making the melt pool boundaries visible in some cases. Light optical microscopy was done on a ZEISS Axioscope 7 instrument with an automated scale which enabled stitching of images of cross sections up 100 mm<sup>2</sup> at × 10 optical zoom. Microstructure evaluation was done on as-polished samples on a Leo Gemini 1550 SEM equipped with field-emission gun. Imaging was done with secondary electron (SE) and backscattered electron (BSE) receivers, depending on the type of image contrast required. X-ray energy dispersive spectroscopy (EDS) for microanalysis was done with the secondary electron receiver coupled with INCA X-sight software for composition analysis. Some samples were also analysed in as-polished state using a Zeiss Gemini SEM 450 scanning electron microscope (SEM) with field-emission gun source for microanalysis. The microscope was fitted with a Bruker Quantax FlatQuad Energy Dispersive X-Ray Spectroscopy (EDX) detector which enables elemental mapping of microstructure at sub-micron resolutions. The X-ray diffraction (XRD) of samples was done on a finely grinded sample (till 2000 grit size) using a Bragg–BrentanoHD X-ray machine equipped with a Cu source ( $K_{\alpha} = 1.5406\text{\AA}$ ) with 40 mA and 45 kV as the generator settings, scanned between 20 and 100° 2θ with a step size of 0.007° and scan step time as 1 s. The XRD patterns were analysed using DIFFRAC.SUITE EVA software by Bruker and the database used for pattern identification was PDF-4+ 2020 database. Heat treatment of some of the samples was conducted in pre-heated resistance furnace with a secondary thermocouple to verify the temperature close to the sample and keep temperature control within ±2°C followed by quenching in cold water. The Vickers hardness testing was done as per ASTM standards E92, E384 on the as-printed and potentially peak-aged specimens on a DuraScan system (from Struers) keeping a load of 0.3 kg, hold time of 10 s and spaced at least five times the indentation dimensions. 16 points (4 ×

4 grids) were taken along both XZ plane and XY plane of each sample and averaged to get the range of hardness values.

### Acknowledgments

The work was conducted in the framework of the Centre for Additive Manufacturing – Metal (CAM<sup>2</sup>) and project ALL-Light, supported by the Swedish Governmental Agency of Innovation Systems (VINNOVA). Sven Bengtsson and Sigurd Berg at Höganäs AB are acknowledged for help procuring the powder and during alloy designing discussions. Ola Lyckfeldt at RISE, Mölndal is acknowledged for doing the powder size distribution analysis for all the alloys. Anton Dahl-Jendelin at RISE Mölndal are acknowledged for discussions during design of experiments for developing printing parameters. Björn Skårman at Höganäs AB is acknowledged for conducting X-ray diffraction experiments and their interpretations. Dmitri Riabov and Tea Bertilsson at Höganäs AB are acknowledged for help with conducting ICP-AES analysis.

### Funding

Funding was provided by VINNOVA (Grant No. 2018-02844) and Lars Nyborg (Grant No. 2016-05175).

### Data availability

Some data that could not be presented in this article is available as supplementary data (mentioned as online resource). Other data generated during this study are available from the corresponding author upon reasonable request.

### Declarations

**Conflict of interest** The authors declare no competing interests with this work.

### Supplementary Information

The online version contains supplementary material available at <https://doi.org/10.1557/s43578-022-00533-1>.

### Open Access

This article is licensed under a Creative Commons Attribution 4.0 International License, which permits use, sharing, adaptation, distribution and reproduction in any medium or format, as long as you give appropriate credit to the original author(s) and the source, provide a link to the Creative Commons licence, and indicate if changes were made. The images or other third party material in this article are included in the article's Creative Commons licence, unless indicated otherwise in a credit line to the material. If material is not included in the article's Creative Commons licence and your intended use is not permitted



by statutory regulation or exceeds the permitted use, you will need to obtain permission directly from the copyright holder. To view a copy of this licence, visit <http://creativecommons.org/licenses/by/4.0/>.

## References

1. D. G. Rogich and G. R. Matos, The global flows of metals and minerals. (2008), <http://pubs.usgs.gov/of/2008/1355/>. Accessed 04 Dec 2020
2. International aluminium institut; European aluminium association; Organisation of european aluminium refiners and remelters, (2009), [https://www.world-aluminium.org/media/filer\\_public/2013/01/15/f0000181.pdf](https://www.world-aluminium.org/media/filer_public/2013/01/15/f0000181.pdf). Accessed 04 Dec 2020
3. J.J. Lewandowski, M. Seifi, Metal additive manufacturing: A review of mechanical properties. *Annu. Rev. Mater. Res.* **46**, 151–186 (2016)
4. D. Gu, W. Meiners, K. Wissenbach, R. Poprawe, Laser additive manufacturing of metallic components: Materials, processes and mechanisms. *Int. Mater. Rev.* **57**(3), 133–164 (2012)
5. Q. Jia, P. Rometsch, P. Kurnsteiner, Q. Chao, A. Huang, M. Weyland, L. Bourgeois, X. Wu, Selective laser melting of a high strength Al–Mn–Sc alloy: Alloy design and strengthening mechanisms. *Acta Mater.* **171**, 108–118 (2019)
6. J.R. Croteau, S. Griffiths, M.D. Rossell, C. Leinenbach, C. Kenel, V. Jansen, D.N. Seidman, D.C. Dunand, N.Q. Vo, Microstructure and mechanical properties of Al–Mg–Zr alloys processed by selective laser melting. *Acta Mater.* **153**, 35–44 (2018)
7. J.H. Martin, B.D. Yahata, J.M. Hundley, J.A. Mayer, T.A. Schae-dler, T.M. Pollock, 3D printing of high-strength aluminium alloys. *Nature* **549**, 365–369 (2017)
8. T. Böllinghaus, H. Herold, C. Cross, *Hot Cracking Phenomena in Welds II* (Springer, New York, 2008)
9. M.H. Ghoncheh, M. Sanjari, A.S. Zoeram, E. Cyr, B.S. Amirkhiz, A. Lloyd, M. Haghsheenas, M. Mohammadi, On the microstruc-ture and solidification behavior of new generation additively manufactured Al–Cu–Mg–Ag–Ti–B alloys. *Addit. Manuf.* **37**, 101724 (2020)
10. S. Kou, A criterion for cracking during solidification. *Acta Mater.* **88**, 366–374 (2015)
11. L. Thijs, K. Kempen, J.-P. Kruth, J.V. Humbeeck, Fine-structured aluminium products with controllable texture by selective laser melting of pre-alloyed AlSi10Mg powder. *Acta Mater.* **61**(5), 1809–1819 (2013)
12. S. Thapliyal, M. Komarasamy, S. Shukla, L. Zhou, H. Hyer, S. Park, Y. Sohn, R.S. Mishra, An integrated computational materials engi-neering-anchored closed-loop method for design of aluminum alloys for additive manufacturing. *Materialia* **9**, 100574 (2020)
13. H. Jones, *Developments in Aluminium Alloys by Solidification at Higher Cooling Rates* (University of Sheffield, Department of Metallurgy, Sheffield, 1978)
14. P.A. Hopper, Melt pool temperature and cooling rates in laser powder bed fusion. *Addit. Manuf.* **22**, 548–559 (2018)
15. H. Jones, Rapid solidification. In *Non-equilibrium processing of materials*, Pergamon, (1999), pp. 23–45.
16. W. Rostoker, R.P. Dudek, C. Freda, R.E. Russell, Fast freezing by atomization for aluminum alloy development. *Int. J. Powder Metall.* **9**(4), 139–148 (1973)
17. T. Uesugi, K. Higashi, First-principles studies on lattice constants and local lattice distortions in solid solution aluminum alloys. *Comput. Mater. Sci.* **67**, 1–10 (2013)
18. A. Unal, Effect of processing variable on particle size in gas atomization of rapidly solidified aluminum powders. *Mater. Sci. Technol.* **3**, 1029–1039 (1987)
19. P. Liu, G. Dunlop, Microhardness measurement of individual AlMnCr powder particles produced by rapid solidification. *Mater. Sci. Eng.* **134**, 1238–1243 (1991)
20. P. Liu, G. Dunlop, L. Arnberg, Microstructural development in a rapidly solidified Al–5Mn–2.5Cr alloy. *Mater. Sci. Eng.* **98**, 437–441 (1988)
21. D. Shechtman, I.A. Blech, The microstructure of rapidly solidi-fied Al<sub>6</sub>Mn. *Metall. Trans.* **16**, 1005–1012 (1985)
22. Midson and H. Jones, Rapidly quenched metals, (1982).
23. J.E. Hatch, *Aluminum: Properties and Physical Metallurgy* (American Society of Metals, Materials Park, 1984)
24. S. Hori, S. Saji and A. Takehara, Quasi-stable phase and crystal grain refinement of quenched and solidified Al–Zr alloy. *Proc. of 4th International Conference on Rapidly Quenched Metal*, vol. 2, pp. 1545–1548, (1981).
25. T. Ohashi, L. Dai, N. Fukatsu, Decomposition characteristics of Al–Mn–Zr alloys rapidly quenched from the melt. *Metall. Trans. A* **17**(5), 799–806 (1986)
26. M. Walbruhl, D. Linder, J. Ågren, A. Borgenstam, Modelling of solid solution strengthening in multicomponent alloys. *Mater. Sci. Eng.* **700**, 301–311 (2017)
27. K.E. Knipling, D.C. Dunand, D.N. Seidman, Criteria for develop-ing castable, creep-resistant aluminum based alloys-a review. *Int. J. Mater. Res.* **97**, 246–265 (2006)
28. K. Saksl, D. Vojtech, H. Franz, Quasicrystal-crystal structural transformation in Al-5wt% Mn alloy. *J. Mater. Sci.* **42**, 7198–7201 (2007)
29. N.T. Aboulkhair, N.M. Everitt, I. Ashcroft, C. Tuck, Reducing porosity in AlSi10Mg parts processed by selective laser melting. *Addit. Manuf.* **1–4**, 77–86 (2014)
30. N.T. Aboulkhair, M. Simonelli, L. Parry, I. Ashcroft, C. Tuck, R. Hague, 3D printing of aluminium alloys: Additive manufactur-ing of aluminium alloys using selective laser melting. *Progr. Mater. Sci.* **106**, 100578 (2019)
31. W. Kurz, D.J. Fischer, Dendrite growth at the limit of stability: Tip radius and spacing. *Acta Metall.* **29**, 11–20 (1981)
32. Y. Du, Y.A. Chang, B. Huang, W. Gong, Z. Jin, H. Xu, Z. Yuan, Y. Liu, Y. He, F.-Y. Xie, Diffusion coefficients of some solutes in fcc

- and liquid Al: critical evaluation and correlation. Mater. Sci. Eng. A **363**(1–2), 140–151 (2003)
33. Z. Cordero, B.E. Knight, C.A. Schuh, Six decades of the Hall–Petch effect—A survey of grain-size strengthening studies on pure metals. Int. Mater. Rev. **61**(8), 495–512 (2016)
  34. Y. Fan, *Precipitation Strengthening of Aluminum by Transition Metal Aluminides* (Worcester Polytechnic Institute, Worcester, 2015)
  35. T.-Y. Huang, C.J. Marvel, P.R. Cantwell, M.P. Harmer, C.A. Schuh, Grain boundary segregation in Al–Mn electrodeposits prepared from ionic liquid. Journal of Material Science **51**, 438–448 (2016)
  36. K.E. Knipling, D.C. Dunand, D.N. Seidman, Nucleation and precipitation strengthening in dilute Al–Ti and Al–Zr alloys. Metall. and Mater. Trans. A **38A**, 2552–2563 (2007)